Fracture behaviour of a rubber nano-modified structural epoxy adhesive: bond gap effects and fracture damage zone

Dong Quan, Neal Murphy, Alojz Ivankovic

www.elsevier.com/locate/ijadhadh

PII: S0143-7496(17)30087-8
DOI: http://dx.doi.org/10.1016/j.ijadhadh.2017.05.001
Reference: JAAD2006

To appear in: *International Journal of Adhesion and Adhesives*

Received date: 23 August 2016
Accepted date: 6 March 2017

Cite this article as: Dong Quan, Neal Murphy and Alojz Ivankovic, Fractur behaviour of a rubber nano-modified structural epoxy adhesive: bond gap effect and fracture damage zone, *International Journal of Adhesion and Adhesives* http://dx.doi.org/10.1016/j.ijadhadh.2017.05.001

Fracture behaviour of a rubber nano-modified structural epoxy adhesive: bond gap effects and fracture damage zone

Dong Quan, Neal Murphy, Alojz Ivankovic*

School of Mechanical and Materials Engineering, University College Dublin, Dublin, Ireland

Abstract

This paper critically examined the fracture behaviour of a rubber-modified, structural epoxy adhesive with various bond gap thicknesses ranging from 0.05 mm to 6 mm. The main and very novel contribution is direct measurement of the fracture process zone, plastic deformation zone and intrinsic fracture energy dissipated in the fracture process zone. The shape and size of the fracture process zone and plastic deformation zone were identified using scanning electron microscope, transmission electron microscope and transmission optical microscope. As the bond gap thickness increased, the fracture energy increased steadily from 2365 J/m^2 of 0.05 mm bond gap thickness to 6289 J/m^2 of 1.6 mm bond gap thickness, and then plateaued. The thickness and failure strain of the fracture process zone remained essentially constant, being approximately 0.052 mm and 0.55 respectively, for different bond gap thicknesses. The intrinsic fracture energy (dissipated in the fracture process zone) appeared to be a material property, which remained approximately 2738 J/m^2. Plastic deformation zone extended through the entire bond gap in thickness and occupied a significant long region in length for all bond gap thicknesses. The effect of bond gap thickness on the fracture energy of the adhesive joints is hence directly attributed to the variation of the plastic deformation energy (dissipated in the plastic deformation zone) with bond gap

thickness.

Keywords

Nano-modified epoxy adhesive, Bond gap thickness, Fracture damage zone, Fracture process zone

1. Introduction

Due to the high fracture energy and good resistance to fracture, the application of rubber nano-modified structural epoxy adhesives has expanded extensively in a wide range of industries including automotive [1, 2] and aerospace [3]. Understanding the fracture behaviour of the nano-modified epoxy adhesives is critical for analysing and improving the adhesive joint integrity. In the fracture of a solid, the irreversible damage process takes place in a region around the crack tip, known as fracture damage zone. The fracture damage zone consists of two regions, the fracture process zone (FPZ) and the plastic deformation zone (PDZ), as shown in Figure 1 (a) [4–6]. The FPZ for rubber-modified adhesives is defined as the region surrounding the crack tip which contains the main fracture processes consisting of rubber cavitation, plastic void growth and shear band yielding. The PDZ is defined as the 'far-field' region that surrounds the FPZ, and consists of mainly plastic deformation. Hence, the fracture energy, G_{IC}, can be divided into two parts, the intrinsic fracture energy consumed in the FPZ, G_0, and the energy dissipated in the PDZ, G_p.

The Mode-I fracture behaviour of rubber-modified epoxy adhesive joints with various bond gap thicknesses (BGT) has been studied widely [7–13] with different results and conclusions presented. An optimum BGT with respect to the fracture

energy of epoxy adhesive joints was observed in [7–10]. A schematic model for explaining the relationship between fracture energy, G_{IC} and bond gap thickness, t, was given in [7], see Figure 1 (b). As the BGT increases, the fracture energy increases steadily to a maximum value, then drops to the value of bulk specimens. It has been suggested that such behaviour, for a modified adhesive system, is due to varying sizes of PDZ that develops ahead of the crack tip [7]. When the BGT is equal to the diameter of the PDZ in the bulk specimens, the PDZ size and G_{IC} are maximised. A different trend was reported in [11–13] that, as the BGT increased, the fracture energy increased then plateaued at a value that is much higher than that of the bulk specimens. Ranade et al. [13] studied the effect of BGT on the fracture of adhesive joints using a tapered bondline thickness double cantilever beam (DCB) specimen. It was found that fracture energies increased until the bondline thickness reached approximately 2.2 mm. Fracture energies plateaued at bondline thicknesses greater than 2.2 mm with no downward trend observed up to 4.5 mm. Cooper et al. [11] studied the effect of BGT on the fracture energy of nano-modified epoxy adhesive joints and presented that the fracture energy increased steadily as the BGT increased from 0.25 mm to 1.3 mm, then remained essentially constant for larger BGT (up to 2.5 mm) without a downward trend. Finite Volume analysis of the tapered double cantilever beam (TDCB) joints with several bondline thicknesses was conducted using a Dugdale type cohesive zone model (CZM) to simulate the fracture. In [11], the BGT effect on the fracture energy was directly attributed to the variation of the stress constraint within the adhesive joint.

Extensive studies, such as [11, 14–20], have been conducted to simulate the fracture of adhesive joints using the CZM. For modelling the fracture of adhesive joints, the CZM has been applied in two ways: (i) the entire adhesive layer is represented by the CZM [17, 18, 21]; (ii) the CZM accounts for the failure mechanisms in the fracture process zone (FPZ) while both the adhesive layer and the adherents were modelled as a continuum [19, 22]. The second type of model is more adequate for

simulating deformation and failure of joints, while the first method remains an over simplification to the adhesive joint fracture [19]. Whom using the second type of model, the total fracture energy, G_{IC}, is divided into two parts, G_0, which is the intrinsic work of fracture associated with the CZM, and G_p, which is the contribution of the plastic deformation energy in the PDZ. The intrinsic fracture energy is given by the area under the traction-separation curve:

$$G_0 = \int_0^{\delta_c} \sigma_c d\delta \tag{1}$$

It was found that the cohesive strength, σ_c and the intrinsic fracture energy, G_0 are the two critical parameters of the CZM, while the shape of the traction- separation curve is considered to be of secondary importance for quasi-static crack growth [23, 24].

Pardoen et al. [19] performed several simulations with different values of σ_c and G_0 for compact tension specimens and TDCB specimens until a very close match was found between the predictions and the experimental data. A single set of σ_c and G_0 was obtained by this inverse method. The numerical results predicted the fracture of adhesive joints with different bond gap thickness using the obtained CZM parameters. In that work, G_0 is taken as a material parameter independent of the local stress state and the change of the adhesive thickness induces constraint effects by affecting the plastic deformation in the adhesive layer, which results in a change of G_p. The opposite conclusion was given by Cooper et al. [11], who modelled the fracture of TDCB joints over a range of bond gap thicknesses and found that when different combinations of σ_c and $G_0 = G_{IC}$ were used, the CZM simulations accurately predicted the fracture of TDCB joints with different BGT. McAuliffe [25, 26] measured σ_c of the adhesive subject to high stress constraint using the joint circumferential deep notch tensile test. The author modelled the fracture of TDCB tests by applying a fixed σ_c (measured experimentally) and varied G_0 for different

BGT TDCB joints. Both the force-displacement relationships and the crack growth traces were predicted quite well when $G_0 \approx G_{IC}$. The observations in [11, 26] pointed to the conclusion that the BGT effect on the fracture of TDCB joints attributed to the variation of the intrinsic fracture energy, while the energy dissipated in the PDZ was negligible.

Based on the literature review, the fracture behaviour of adhesive joints with different BGTs is not fully understood. The measurement of the FPZ and PDZ is critical to fully understand the BGT effects on the fracture behaviour of adhesive joints. In this work, the fracture behaviour of a nano-modified structural epoxy adhesive with various BGTs is investigated and the shape and size of the PDZ and FPZ are identified.

2. Experimental Work

2.1. Adhesive

The adhesive is an experimental grade, nano-toughened structural epoxy adhesive, which was supplied in the form of a one-component paste by Henkel Ireland. This adhesive is toughened by two types of core-shell rubber (CSR) nanoparticles; CSR-L with an average diameter of 203 nm (Zeon F351 FROM Nippon Zeon Chemicals) and CSR-S with an average diameter of 74 nm (Kane Ace MX153 Kaneka). The volume fractions of the CSR-L and CSR-S are 22 vol.% and 16 vol.% respectively. The adhesive curing schedule is 90 minutes at 180°C.

2.2. TDCB Joint Preparation and Testing

The TDCB substrates were manufactured from aluminium alloy (Al2014-T6) plates using a CNC machine according to the British standard [27] and a schematic of the TDCB geometry is shown in Figure 2 (a). The bonding surfaces of the substrates were treated to ensure that crack grows cohesively in the adhesive layer. The

surface treatment was conducted in NIACE Centre, Bombardier Aerospace (Belfast). It consisted of acetone degreasing with subsequent grit blasting. Following the grit blasting, the substrates were rinsed clear with running hot water, dried, and wiped with acetone. The substrates were then placed into an air-circulating oven at 50°C for 30 minutes to remove the moisture. Finally, a Stuart-Bengough chromic acid anodising process was employed on the bonding surfaces. The joints were bonded after the substrates were anodised and dried. A PTFE film with a thickness of 12.5 μm was placed in the adhesive layer at the loading end to introduce a sharp initial crack. This is shown as the red line in Figure 2 (a). The distance between loading line and the front of the initial crack was 100 mm. Two spacers were placed at each end of the joint to obtain the desired BGT. The BGTs of 0.05 mm, 0.1 mm, 0.55 mm, 1 mm, 1.6 mm, 2.4 mm, 3 mm, 4 mm and 6 mm were used here. The assembled joints were placed into a pre-heated oven at 180 °C for 90 minutes to cure. After the curing, the joints were left in the oven to cool down slowly (from 180°C to room temperature) to minimise residual stresses generated in the adhesive joints. After that, all the spacers were carefully removed.

The TDCB tests were carried out on a screw driven testing machine (Hounsfield H50KS) at a loading rate of 0.3 mm/min at room temperature. The joints were unloaded when the crack length reached 190 mm. At this stage, sufficient data has been collected to calculate the fracture energy and a fully developed fracture damage zone had been formed at the crack tip. The compliance of the machine and loading rigs was estimated by fitting an aluminium block into the loading rigs and loading past the maximum force in the TDCB test. The measured displacement was corrected based on the measured compliance. The corrected beam theory described in [27] was used to calculate the fracture energy.

2.3. Microscopy

The fracture surfaces of the TDCB specimens were imaged using a scanning electron microscope equipped with a field-emission gun (SEM, FEI Quanta 3D) under an acceleration voltage of 5 kV. The samples were gold sputter coated at a current of 30 mA for 30 seconds to get an approximately 10 nm thick gold layer. The images were taken along the centre of the sample in a direction parallel to crack growth at a distance from the initial crack of between 40 mm and 50 mm.

To investigate the shape and size of the fracture damage zone, a transmission optical microscope (TOM, Nikon E80i Orina) and a reflective optical microscope (ROM, IMXZ Stereomicroscope from Brunel Microscope) were used. The samples were taken from the centre of the TDCB specimens perpendicular to the fracture plane and parallel to the crack direction. Samples from two positions on the pre-tested TDCB specimens, which are shown as Position-a and Position-b in Figure 2 (b), were imaged. The samples from Position-a contained a separated fracture surface, while the samples from Position-b contained the crack tip with a fully developed fracture damage zone. The samples were ground and polished to a thin section with an approximate thickness of 180 μm by following the technique described described in [28].

The fracture subsurfaces were imaged using a transmission electron microscope (TEM, FEI Tecnai G2 20). The samples taken from centre-plane at Position-a were firstly mounted using the Agar100 Epoxy Resin (from Agar Scientific) to protect the fracture surface morphology. Then, thin sections with a thickness approximately 100 nm were machined by cryo-microtome (LEICA EM UC6) and imaged using TEM.

3. Results and Discussion

3.1. TDCB Test Results

The force-displacement curves from the TDCB tests are shown in Figure 3. It should be noted that all the curves except for the BGT equals 6 mm are shifted to the right for ease of observation. Stable crack propagation occurred for the BGT below 4 mm. For the BGT of 4 mm and 6 mm, the TDCB joints fractured dynamically after the force reached the maximum value. The square points on the force-displacement curves correspond to the crack initiation points. They were not obtained for the specimens with BGTs of 4 mm and 6 mm due to the difficulty in identifying the crack initiation accompanied with the large BGTs. It was observed that the crack initiation forces have similar values for different BGTs, and the difference between the crack initiation force and the crack propagation force decreased as the BGT decreased, and finally disappeared when the BGT was 0.05 mm.

Figure 4 depicts the crack growth process of a typical 1.6 mm BGT TDCB joint. It is found that the the opening of the initial crack front took place as the load increased, which was followed by the crack initiation by a small slightly kinked increment. After the crack initiation, many secondary micro-cracks, which were also observed in [29], initiated and expanded at the far-field region in front of the crack tip. The micro-cracks grew and eventually coalesced with the main crack as the load increased. The main crack (continuous crack) propagated forward when an approximately 5-10 mm long array of micro-cracks was developed ahead of the crack tip. In the current work, the front of the region with micro-cracks was treated as the crack tip.

Figure 5 shows the curves of the fracture energy versus crack length for different BGT specimens. It is found that the fracture energy levelled off for crack lengths

above 110 mm for all BGT except 0.05 mm which was levelled throughout. The initial point for a crack length of 100 mm is the crack initiation point and it is found that the crack initiation energies have similar values for the range of BGTs investigated, varied between 2500-3000 J/m^2.

Figure 6 shows the fracture energy as a function of BGT. The fracture energy of the TDCB specimens with a BGT of less than 4 mm is the average of the fracture propagation energy, while the fracture energy for the BGTs of 4 mm and 6 mm (which fractured rapidly) is calculated using the maximum load. A steep increase in the fracture energy is observed as the BGT increased from 0.05 mm to 0.1 mm followed by a less steep increase for the BGT in the range of 0.1 mm to 1.6 mm. The fracture energy plateaus at a BGT of approximately 1.6 mm. No downward trend was observed as the BGT increased up to 6 mm.

3.2. Fracture Surface Topography

Figure 7 shows the fracture surfaces of the TDCB joints, which exhibited stable crack propagation. Cohesive failure is observed when the BGT is greater than 0.1 mm. For small BGT of 0.05 mm and 0.1 mm, the failure mode was a mixture of cohesive and interfacial failures. This was caused by the lack of adhesive between the substrates for cohesive material separation.

Figure 8 contains typical SEM images of the TDCB fracture surfaces. It was revealed that the fracture surfaces of different BGT specimens are covered with voids generated by CSR debonding or cavitation, which can be identified as circular features. We have no direct evidence of debonding or cavitation of CSRs. Given that no particles remain on the fracture surface and the general view is that CSR cavitated [30, 31], we will refer to voids generated by CSRs as a results of rubber cavitation throughout the work. The size of the large voids was measured using ImageJ [32] software. About 700 measurements were taken for each BGT. No

statistical difference in the size of the voids is observed for different BGTs. The mean diameter of the large voids varied between 260-270 nm for all BGTs. This indicates that the failure strain of the FPZ was more or less the same for different BGTs. The size of the smaller voids from CSR-S was not measured due to inadequate image resolution.

3.3. Fracture Damage Zone

3.3.1. Plastic Deformation Zone (PDZ)

Damage occurring in the adhesive layer will affect its morphology and transparency in a TOM image. In the fracture of a rubber toughened epoxy adhesive, the plastic void growth and shear band yielding normally occur within the FPZ [33–35] while only bulk plasticity and shear band yielding [36] occur within the PDZ. Therefore, in a TOM image, the PDZ has a darker colour than the non-damaged adhesive layer due to the presence of plastic deformation, and the FPZ has a darker colour than the PDZ due to a higher density of damage [35].

Figure 9 shows the TOM images of the samples taken from Position-a (except the one for 4 mm BGT). The sample for the 4 mm BGT specimen (dynamic failure) was taken from the position of the crack length between 105-110 mm, where the crack grew slowly before the dynamic failure of the joints. The top brighter image is taken from the section with the PTFE film insert, which is undamaged. It can be seen that images of fractured sections for all BGTs have a darker appearance when compared with the top image. This implies the existence of plastic deformation, which usually occur in the PDZ. It is found that the PDZ occupies the entire thickness of the adhesive layer for the TDCB joints with different BGTs. The interface between the substrate and the adhesive layer is not visible for the 0.05 mm and the 0.1 mm BGT samples due to the high damage density in the adhesive layer in these two cases. The depth of the PDZ increases with no downward trend observed as the BGT

increases up to 4 mm.

Figure 10 shows the TOM images of the samples taken from Position-b under bright field. The images are made up of three to four sub-images with visible lines where two sub-images are joined. The blue dashed lines indicate the crack tip and the red dashed line indicates the PDZ front. The region on the right hand side of the red dashed line is the adhesive layer without damage. In the images for 0.05 mm and 0.1 mm BGT, the crack fronts are not visible.

The ImageJ software [32] was used to measure the PDZ sizes in Figure 10 and the measurements along with the fracture energy are shown in Table 1. The PDZ thickness equals the BGT in all cases, and the PDZ length remains more or less constant (between 10-13 mm) as the BGT increases from 0.55 mm to 3 mm. A big difference in the shape and size of the PDZ between the TDCB joints and the bulk specimens [37] was observed, which could be attributed to the complex stress state in the TDCB joints caused by the presence of the stiff substrates, which promoted the extension of the PDZ in front of the crack tip.

3.3.2. Fracture Process Zone (FPZ)

In Figure 10, a very dark area surrounding the crack line was observed in the fractured part of the adhesive layer for BGTs above 0.1 mm, while the entire adhesive layer is very dark for BGT below 0.1 mm. Figure 11 presents the ROM images of the same samples. The white 'lines' observed in the images correspond to the dark areas in Figure 10. A darker colour in the TOM images and a lighter colour in the ROM images indicate a higher density of damage.

Figure 12 shows the TOM images of the samples taken from Position-b under cross polarised light. Bright birefringence is observed mainly in the region with higher damage density. Only small amount of scattered bright birefringence occurs in the rest of the crack tip region. The bright birefringence typically indicates matrix shear

yielding or shear bands, which causes the orientation of the epoxy molecules [38, 39].

Figure 13 presents the TEM images of the fracture subsurface of the TDCB specimens, while Figure 14 shows the image for the 1.6 mm BGT specimen with higher magnifications. The red arrows indicate the microtoming directions. A large number of voids are observed in the region with higher damage density observed in Figures 10 and 11. The density of the voids decreases with the distance/depth from the fracture surface and eventually the voids are no longer visible. The depth of the voided region can not be measured for a high level of certainty. However, it seems to be constant for all BGTs and reasonably close to 35-45 μm. This gives a total thickness of voided region of around 70-90 μm, which is close to the thickness of the high density damage region.

Based on the microscopy work, the high damage density region around the fracture plane is identified as the FPZ, associated with particle debonding or cavitation, plastic void growth, shear band yielding and final material separation.

The thickness of the FPZ for BGT above 0.1 mm was measured from both Figures 10 and 11 using the ImageJ software, and the measurements agreed well with each other. Ten measurements were conducted for each sample and the average thickness is summarised in Table 2. It was found that the thickness of this area is approximately 0.08 mm for all BGTs. This initial thickness of the materials layer that undergoes intrinsic damage process which eventually constitute the FPZ can be calculated as follows.

Based on the measurement of the void size on the fracture surfaces, the failure strain could be approximated as:

$$\varepsilon_f = \frac{r_f - r_0}{r_0} \qquad (2)$$

where r_f is the final radius of the voids, 131.5 nm (the average value for all BGTs) and r_0 is the original radius of rubber core (particle size), 84.8 nm, which was measured in previous work [37]. The failure strain within the FPZ is therefore approximately 0.55. It should be noted that this is the strain around the particle on the fracture surface. If it is assumed that the plastic voids grow evenly across the FPZ, the approximate thickness of the initial FPZ is 0.08/(1+0.55)=0.052 mm. It is reasonable to assume that the intrinsic fracture energy that dissipated in the FPZ equals the fracture energy of the 0.052 mm BGT TDCB specimens; this was obtained by polynomial interpolation of the G_{IC} versus BGT curve, as shown in Figure 15, to be 2738 J/m^2. Hence the intrinsic fracture energy of the adhesive joints remains around 2738 J/m^2 for all BGTs, which is quite close to the measured crack initiation energy for different BGTs, see Figure 5.

3.4 Discussion

According to the experimental observations, the fracture process evolution for TDCB joints is depicted in Figure 16, which could be divided into mainly three stages according to the force-displacement relationship: Stage 1, the FPZ initiates and grows ahead of the initial crack as the force increases, followed by crack initiation when the force reaches the initiation value. The sharp initial crack might be significantly blunted due to the high ductility of the adhesive in this stage. Stage two, plasticity occurs around the FPZ leading to the development of a large scale PDZ, which corresponds to the nonlinear increase of the force as the displacement increases, see Figure 3. In this stage, many micro-cracks initiate and grow inside the FPZ. Stage 3, the fracture damage zone is fully developed, the micro-cracks coalesced and the crack starts to propagate along the length of the joint with a constant force until the final failure. The fracture energy of the adhesive joint consists of two contributions, the intrinsic fracture energy dissipated in the FPZ and the plastic energy dissipated in the PDZ. The FPZ energy corresponds to the crack

initiation energy while the PDZ energy corresponds to the energy-difference between the constant crack-propagation energy and the crack-initiation energy.

Many observations described earlier can now be explained: Firstly, similar values of crack initiation force and energy are observed for different BGTs, see Figures 3 and 5. This is because crack initiation energy consists of the energy dissipated in the FPZ. The FPZ failure strain and the FPZ thickness are found to be more or less the same for different BGTs, so the crack initiation energy remains essentially constant for all BGTs and hence it does appear to be the material property. Secondly, this also explains why the crack propagated under plateaued force directly once the crack initiated for the 0.05mm BGT specimens. In this case, the BGT is smaller than the FPZ thickness, hence the entire adhesive layer is occupied by the FPZ and no PDZ developed. Lastly, for the BGTs below the FPZ thickness of 0.052 mm, a steep decrease in the fracture energy is observed (see Figure 6). In this case, insufficient material is available to develop the full-size FPZ. As a consequence, fracture mode is a mixture of cohesive and interfacial failures where many spots of aluminium substrates were seen on the fracture surface of 0.05 mm BGT TDCB joints in Figure 7.

The BGT effect on the fracture behaviour of the adhesive joints may be therefore summarised as follows. When the BGT is less than the FPZ thickness of approximately 0.052 mm, mixed cohesive-interfacial failure takes place. The fracture energy is very sensitive to the BGT under this condition. For BGTs above the FPZ thickness, the fracture mode changes to cohesive failure and the fracture energy increases linearly as the BGT increases. As the BGT increases, the increase in total fracture energy may be attributed to the increase in the energy dissipated in the PDZ, while the FPZ size and the FPZ energy remains constant. After the BGT increases above 1.6 mm, the fracture energy plateaus due to PDZ energy contributions also levelling off. The fracture changes from stable to dynamic crack-

propagation for BGT above 3 mm with the maximum fracture energy remaining the same as the plateaued value.

4. Conclusions

This paper critically examined the effects of BGT on the damage and fracture behaviour of CSR modified epoxy adhesive. The main and very novel contribution of the paper is direct measurement of the FPZ and the intrinsic fracture energy. The varying fracture behaviour of the nano-modified structural epoxy adhesive with different BGTs is attributed to the variation of the plastic deformation energy under different stress constraint. The intrinsic fracture energy remains constant for different BGTs, which appears to be the material property. It should be noted that the identification of FPZ and intrinsic fracture energy as a material property indicates a breakthrough in linking TDCB and other fracture test method, such as single end notch three-point bending test. Further work will combine current experimental observations with numerical simulations to predict the TDCB experiments and to link the TDCB test with the 3PB test.

Acknowledgements

The project was jointly supported by the China Scholarship Council and Henkel (Ireland), whose financial assistance is gratefully acknowledged. We would like to acknowledge Bombardier Aerospace (Belfast) for conducting the Stuart-Bengough chromic acid anodising on the bonding surfaces.

Appendix-Acronyms

TDCB - Tapered Double Cantilever Beam Test
FPZ - Fracture Process Zone
PDZ - Plastic Deformation Zone
BGT - Bond Gap Thickness of the Adhesive Layer

CSR - Core Shell Rubber Particles

CZM - Cohesive Zone Model

SEM - Scanning Electron Microscope

TEM - Transmission Electron Microscope

TOM - Transmission Optical Microscope

ROM - Reflective Optical Microscope

References

[1] R. B. Jones, Overview of North American structural adhesives in transportation, Adhesives and Sealants Industry 17 (9) (2010) 18–19.

[2] E. H. Cordes, Adhesives in the automotive industry, in: A.Pizzi, K.L.Mittal (Eds.), Handbook of adhesive technology-Revised and Expanded, CRC Press, New York, 2003, pp. 999–1016.

[3] E. M. Petrie, Adhesives for the assembly of aircraft structures and components: Decades of performance improvement, with the new applications of the horizon, Metal Finishing 106 (2) (2008) 26–31.

[4] K. B. Broberg, Crack-growth criteria and non-linear fracture mechanics, Journal of the Mechanics and Physics of Solids 19 (6) (1971) 407–418. doi:10.1016/0022-5096(71)90008-1.

[5] K. B. Broberg, Cracks and fracture, Academic Press, London, 1985.

[6] M. F. Kanninen, C. H. Popelar, Advanced fracture mechanics, Oxford University Press (New York), 1985.

[7] A. J. Kinloch, S. J. Shaw, The fracture resistance of a toughened epoxy adhesive, The Journal of Adhesion 12 (1) (1981) 59–77. doi:10.1080/00218468108071189.

[8] C. Yan, Y. W. Mai, Q. Yuan, L. Ye, J. Sun, Effects of substrate materials on fracture toughness measurement in adhesive joints, International Journal of Mechanical Sciences 43 (9) (2001) 2091–2102. doi: 10.1016/S0020-7403(01)00030-3.

[9] D. B. Lee, T. Ikeda, N. Miyazaki, N. S. Choi, Fracture behavior around a crack tip in rubber-modified epoxy adhesive joint with various bond thicknesses, Journal of Materials Science Letters 22 (3) (2003) 229–233. doi:10.1023/A:1022218530150.

[10] D. B. Lee, T. Ikeda, N. Miyazaki, N. S. Choi, Effect of bond thickness on the fracture toughness of adhesive joints, Journal of Engineering Materials and Technology 126 (1) (2004) 14–18. doi:10.1115/1.1631433.

[11] V. Cooper, A. Ivankovic, A. Karac, D. McAuliffe, N. Murphy, Effects of bond gap thickness on the fracture of nano-toughened epoxy adhesive joints, Polymer 53 (24) (2012) 5540–5553. doi:10.1016/j.polymer.2012. 09.049.

[12] S. Azari, M. Papini, J. K. Spelt, Effect of adhesive thickness on fatigue and fracture of toughened epoxy joints. Part I: Experiments, Engineering Fracture Mechanics 78 (1) (2011) 153–162. doi:10.1016/j.engfracmech. 2010.06.025.

[13] S. R. Ranade, Y. Guan, D. C. Ohanehi, J. G. Dillard, R. C. Batra, D. A. Dillard, A tapered bondline thickness double cantilever beam (DCB) specimen geometry for combinatorial fracture studies of adhesive bonds, International Journal of Adhesion and Adhesives 55 (0) (2014) 155–160. doi:10.1016/j.ijadhadh.2014.08.006.

[14] D. Alvarez, B. R. K. Blackman, F. J. Guild, A. J. Kinloch, Mode I fracture in adhesively-bonded joints: A mesh-size independent modelling approach using cohesive elements, Engineering Fracture Mechanics 115 (0) (2014) 73–95. doi:10.1016/j.engfracmech.2013.10.005.

[15] S. Azari, M. Papini, J. Spelt, Effect of adhesive thickness on fatigue and fracture of toughened epoxy joints part ii: Analysis and finite element modelling, Engineering Fracture Mechanics 78 (1) (2011) 138–152. doi: 10.1016/j.engfracmech.2010.07.006.

[16] C. Sun, M. D. Thouless, A. M. Waas, J. A. Schroeder, P. D. Zavattieri, Ductile-brittle transitions in the fracture of plastically deforming, adhesively bonded structures. Part II: Numerical studies, International Journal of Solids and Structures 45 (17) (2008) 4725–4738. doi:10.1016/j. ijsolstr.2008.04.007.

[17] T. Ferracin, C. M. Landis, F. Delannay, T. Pardoen, On the determination of the cohesive zone properties of an adhesive layer from the analysis of the wedge-peel test, International Journal of Solids and Structures 40 (11) (2003) 2889–2904. doi:10.1016/S0020-7683(03)00076-3.

[18] A. Karac, B. R. K. Blackman, V. Cooper, A. J. Kinloch, S. R. Sanchez, W. S. Teo, A. Ivankovic, Modelling the fracture behaviour of adhesively- bonded joints as a function of test rate, Engineering Fracture Mechanics 78 (6) (2011) 973–989. doi:10.1016/j.engfracmech.2010.11.014.

[19] T. Pardoen, T. Ferracin, C. M. Landis, F. Delannay, Constraint effects in adhesive joint fracture, Journal of the Mechanics and Physics of Solids 53 (9) (2005) 1951–1983. doi:10.1016/j.jmps.2005.04.009.

[20] Q. D. Yang, M. D. Thouless, Mixed-mode fracture analyses of plastically-deforming adhesive joints, International Journal of Fracture 110 (2) (2001) 175–187. doi:10.1023/A:1010869706996.

[21] Q. D. Yang, M. D. Thouless, S. M. Ward, Numerical simulations of adhesively-bonded beams failing with extensive plastic deformation, Journal of the Mechanics and Physics of Solids 47 (6) (1999) 1337–1353. doi:10.1016/S0022-5096(98)00101-X.

[22] Z. Tukovic, The effect of constraint on the fracture toughness of adhesively bonded joints, in: 32nd Annual Meeting of the Adhesion Society, Savannah, GA, 2009.

[23] J. W. Hutchinson, A. G. Evans, Mechanics of materials: top-down approaches to fracture, Acta Materialia 48 (1) (2000) 125–135. doi:10.1016/ S1359-6454(99)00291-8.

[24] M. Alfano, F. Furgiuele, A. Leonardi, C. Maletta, G. H. Paulino, Mode-I fracture of adhesive joints using tailored cohesive zone models, International Journal of Fracture 157 (1-2) (2009) 193–204. doi:10.1007/ s10704-008-9293-4.

[25] D. McAuliffe, A. Karac, N. Murphy, A. Ivankovic, The measurement of damage initiation, particle adhesion and cohesive strength from traction displacement curves of a nano-toughened epoxy, International Journal of Adhesion and Adhesives 70 (2016) 62–73. doi:10.1016/j.ijadhadh. 2016.04.014.

[26] D. McAuliffe, Fracture toughness characterization of a nano-modified structural polymers, Ph.D. thesis, University College Dublin (August 2012).

[27] BS 7991:2001, Determination of the mode I adhesive fracture energy, GIC, of structural adhesives using the double cantilever beam (DCB) and tapered double cantilever beam (TDCB) specimens, British Standard Institute (2001).

[28] A. S. Holik, R. P. Kambour, D. G. Fink, S. Y. Hobbs., Microstructure Science 7

(1979) 357–367.

[29] D. Purslow, Matrix fractography of fibre-reinforced epoxy composites, Composites 17 (4) (1986) 289–303. doi:10.1016/0010-4361(86)90746-9.

[30] A. J. Kinloch, S. J. Shaw, D. A. Tod, D. L. Hunston, Deformation and fracture behaviour of a rubber-toughened epoxy: 1. Microstructure and fracture studies, Polymer 24 (10) (1983) 1341–1354. doi:10.1016/0032-3861(83)90070-8.

[31] J. Chen, A. J. Kinloch, S. Sprenger, A. C. Taylor, The mechanical properties and toughening mechanisms of an epoxy polymer modified with polysiloxane-based core-shell particles, Polymer 54 (16) (2013) 4276–4289. doi:10.1016/j.polymer.2013.06.009.

[32] W. S. R. Imagej., http://rsb.info.nih.gov/ij/, imagej, US National Institutes of Health, Bethesda, Maryland, USA, 1997-2012.

[33] Y. Huang, A. J. Kinloch, Modelling of the toughening mechanisms in rubber-modified epoxy polymers, Journal of Materials Science 27 (10) (1992) 2753–2762. doi:10.1007/BF00540702.

[34] Y. Huang, A. J. Kinloch, Modelling of the toughening mechanisms in rubber-modified epoxy polymers, Journal of Materials Science 27 (10) (1992) 2763–2769. doi:10.1007/BF00540703.

[35] R. A. Pearson, A. F. Yee, Influence of particle size and particle size distribution on toughening mechanisms in rubber-modified epoxies, Journal of Materials Science 26 (14) (1991) 3828–3844. doi:10.1007/BF01184979.

[36] P. Martiny, F. Lani, A. Kinloch, T. Pardoen, Numerical analysis of the energy contributions in peel tests: A steady-state multilevel finite element approach, International Journal of Adhesion and Adhesives 28 (45) (2008) 222–236. doi:10.1016/j.ijadhadh.2007.06.005.

[37] D. Quan, A. Ivankovic, Effect of core-shell rubber (CSR) nano-particles on mechanical properties and fracture toughness of an epoxy polymer, Polymer 66 (2015) 16–28. doi:10.1016/j.polymer.2015.04.002.

[38] P. Dittanet, R. A. Pearson, Effect of silica nanoparticle size on toughening mechanisms of filled epoxy, Polymer 53 (9) (2012) 1890–1905. doi:10. 1016/j.polymer.2012.02.052.

[39] D. J. Bray, P. Dittanet, F. J. Guild, A. J. Kinloch, K. Masania, R. A. Pearson, A. C. Taylor, The modelling of the toughening of epoxy polymers via silica nanoparticles: The effects of volume fraction and particle size, Polymer 54 (26) (2013) 7022–7032. doi:10.1016/j.polymer.2013.10. 034.

Table 1: Comparison of FDZ size and G_{IC} of TDCB joints with different BGTs

BGT (mm)	0.05	0.1	0.55	1.0	1.6	2.4	3.0	4.0
PDZ length (mm)	*	*	11.7	13.0	12.9	13.4	10.1	*
PDZ thickness (mm)	0.05	0.1	0.55	1.0	1.6	2.4	3.0	4
PDZ area (mm^2)	*	*	6.44	13.00	20.64	32.16	30.30	*
G_{IC} (J/m^2)	2365	2827	4042	4688	5595	5518	5744	5709

Table 2: Thickness of the FPZ in TDCB specimens

BGT (mm)	0.55	1.0	1.6	2.4	3.0
FPZ thickness (mm)	0.08±0.01	0.07±0.01	0.08±0.01	0.09±0.01	0.08±0.01

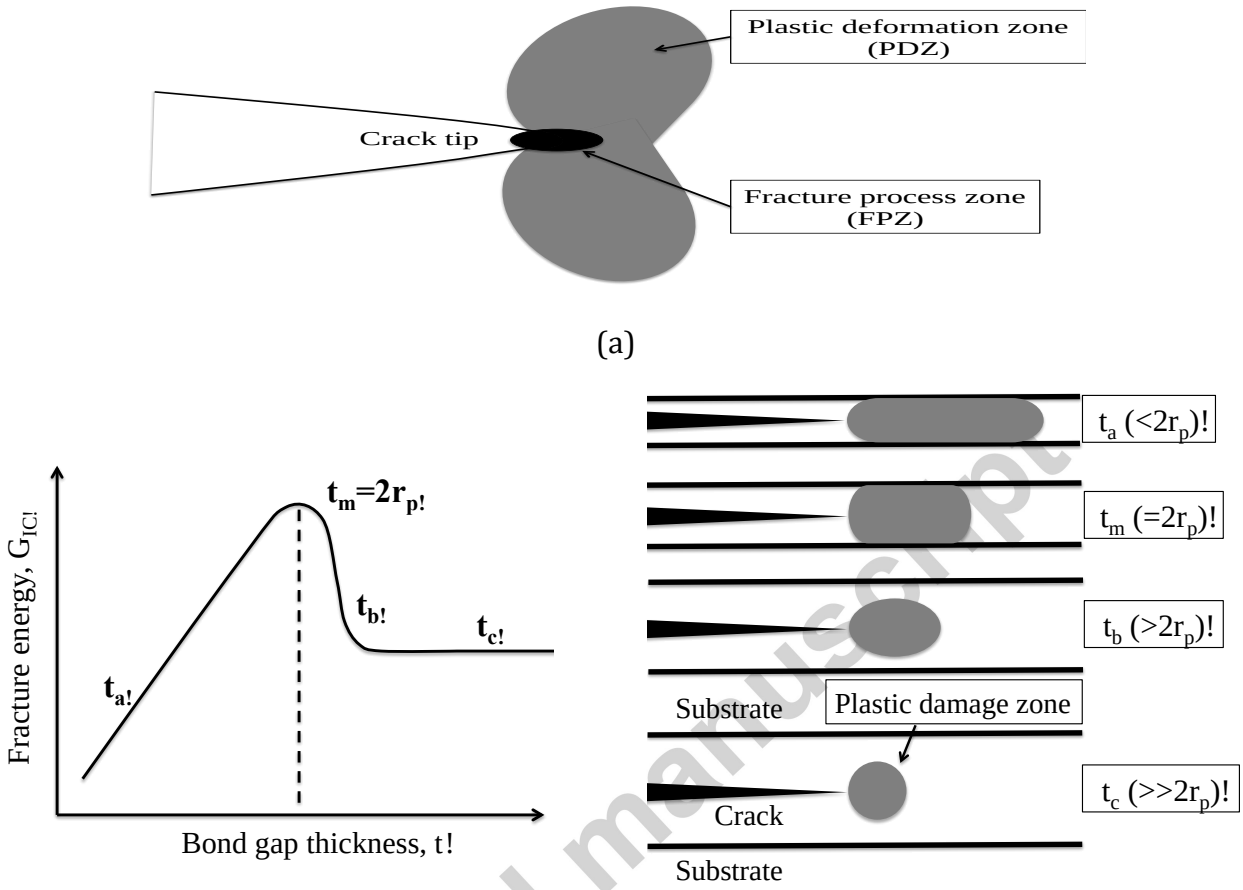

Figure 1: The schematic (a) of the fracture damage zone [5]; (b) for explaining the relationship between G_{IC} and BGT from [7]. r_p is the radius of the PDZ in the bulk specimens.

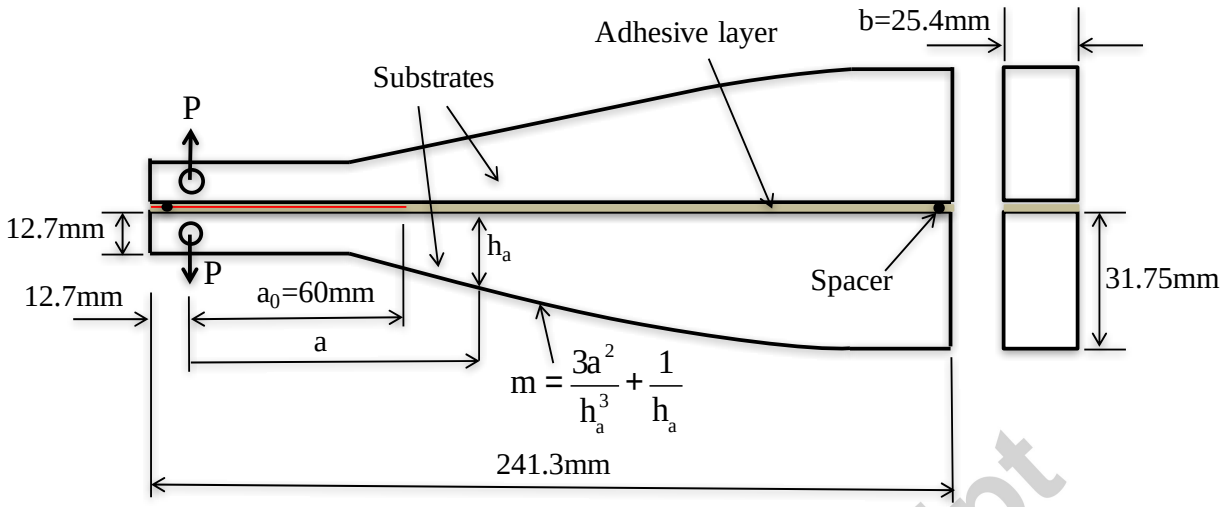

(a)

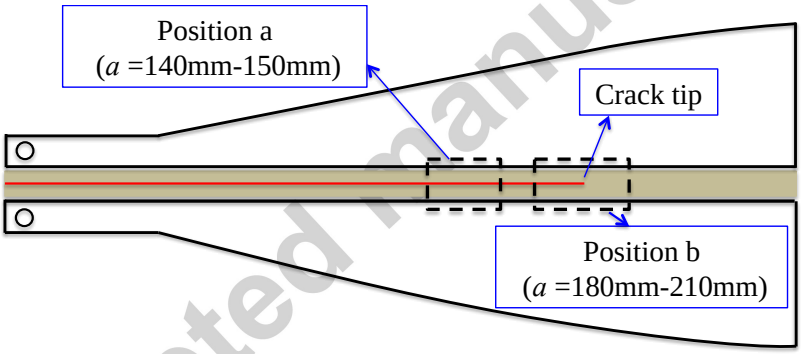

(b)

Figure 2: (a) Geometry of the TDCB specimen; (b) The positions of samples used for microscopy.

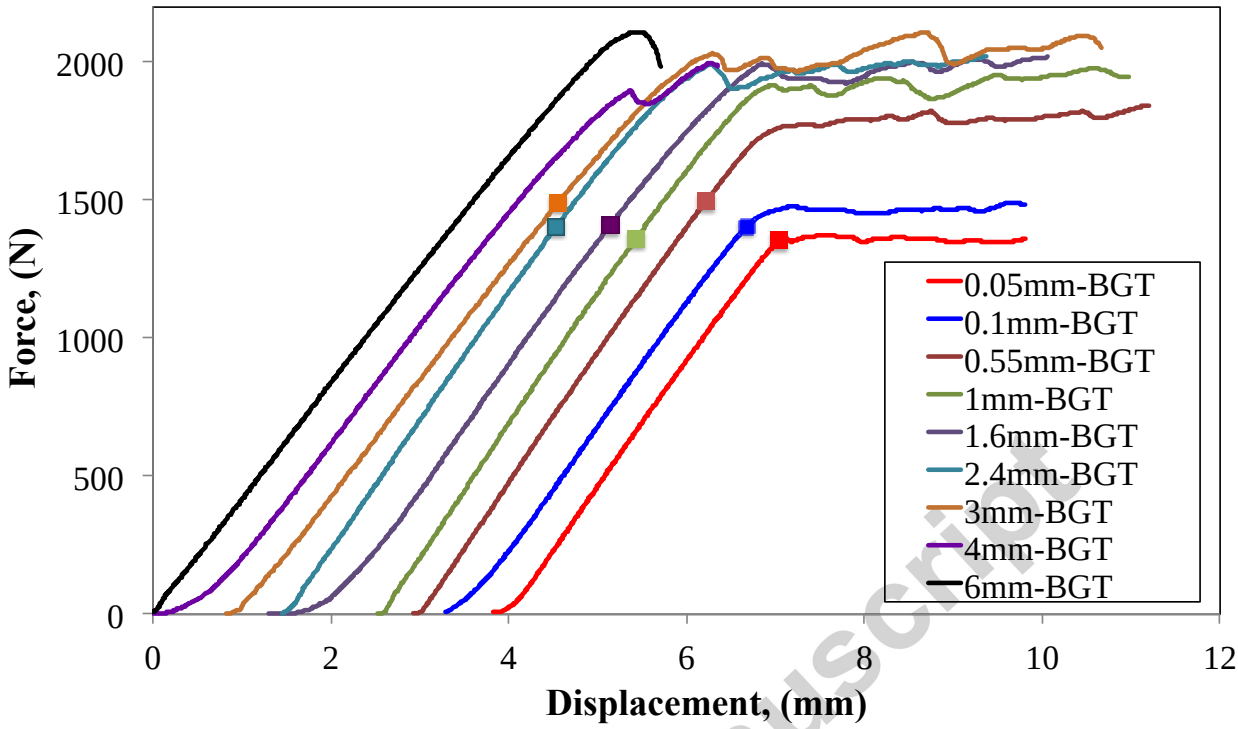

Figure 3: The force-displacement curves of the TDCB tests. The curves for all specimens except for the BGT of 6 mm are shifted to the right to enable them to be more easily observed. The square points on the curves represent the crack initiation points.

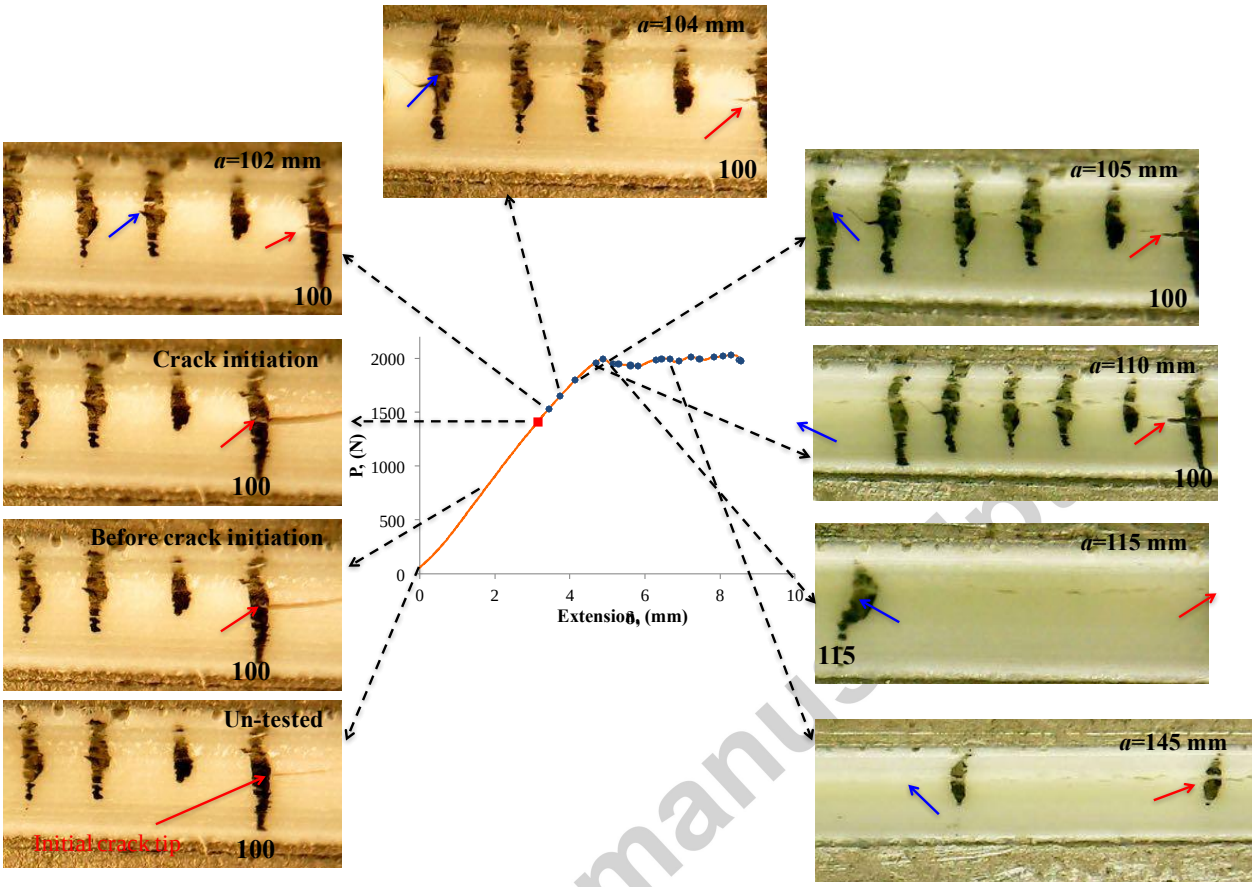

Figure 4: Evolution of the crack tip region for a typical TDCB test (BGT = 1.6 mm). Note that the crack growth direction is from right to left. Red arrows point to the location of continuous crack tip and blue arrows point to location of the front of the micro-cracks array in each image. *a* is the crack length; the distance between the front of the micro-cracks and the loading line.

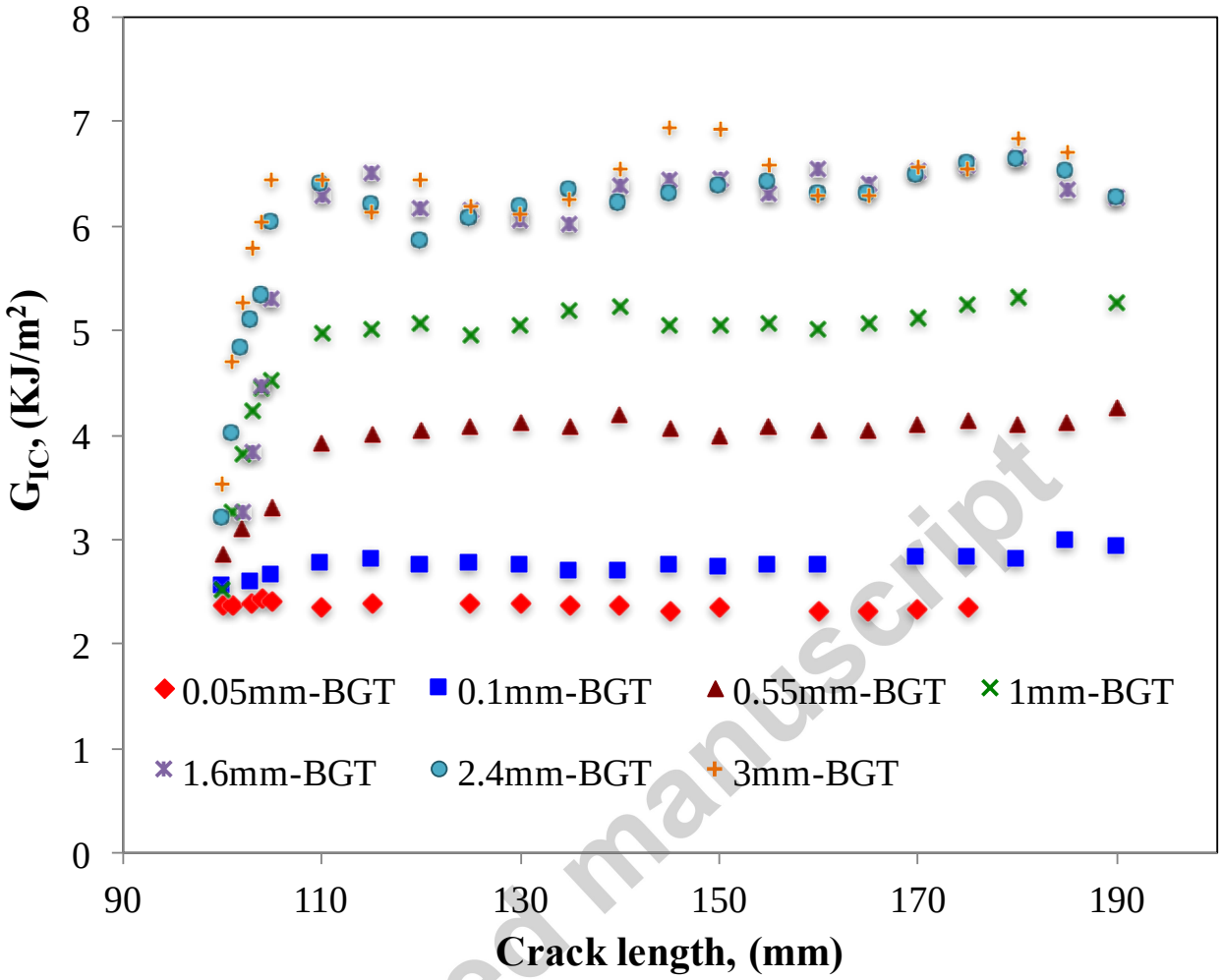

Figure 5: Fracture energy versus crack length for TDCB specimens having varied BGTs.

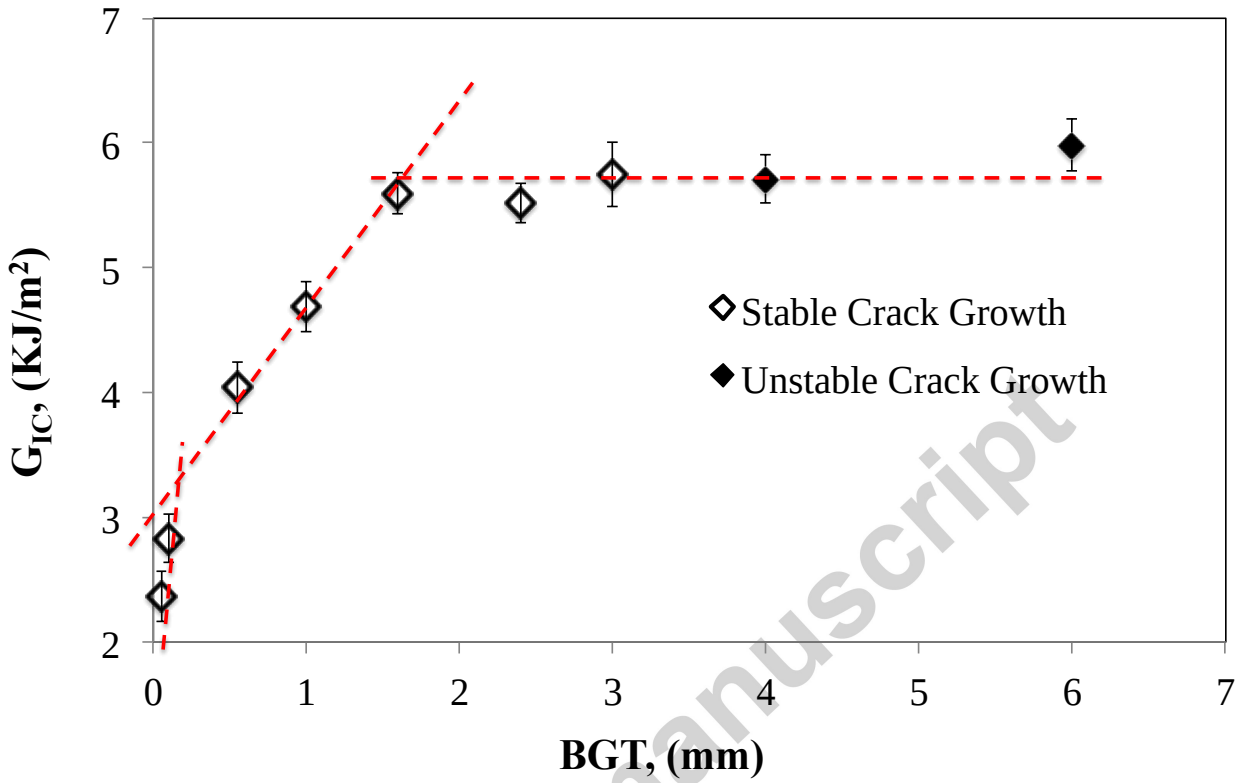

Figure 6: Fracture energy versus the BGT. The red dash lines indicate the variation trend of the fracture energy with the BGT.

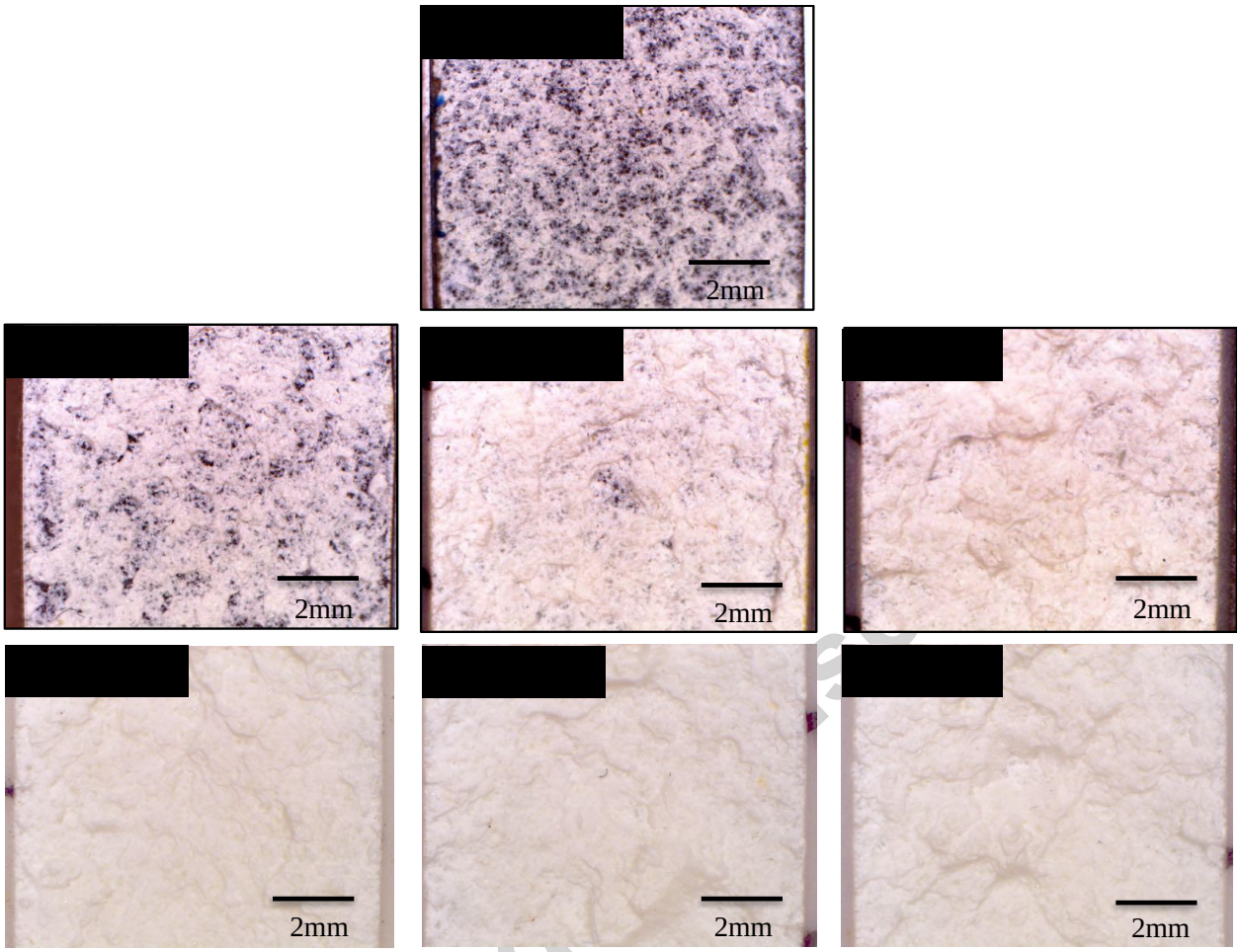

Figure 7: Fracture surfaces of different BGT TDCB specimens having stable crack propagation. Dark spots in "0.05mm BGT" and "0.1mm BGT" figures are the surfaces of the aluminium substrates.

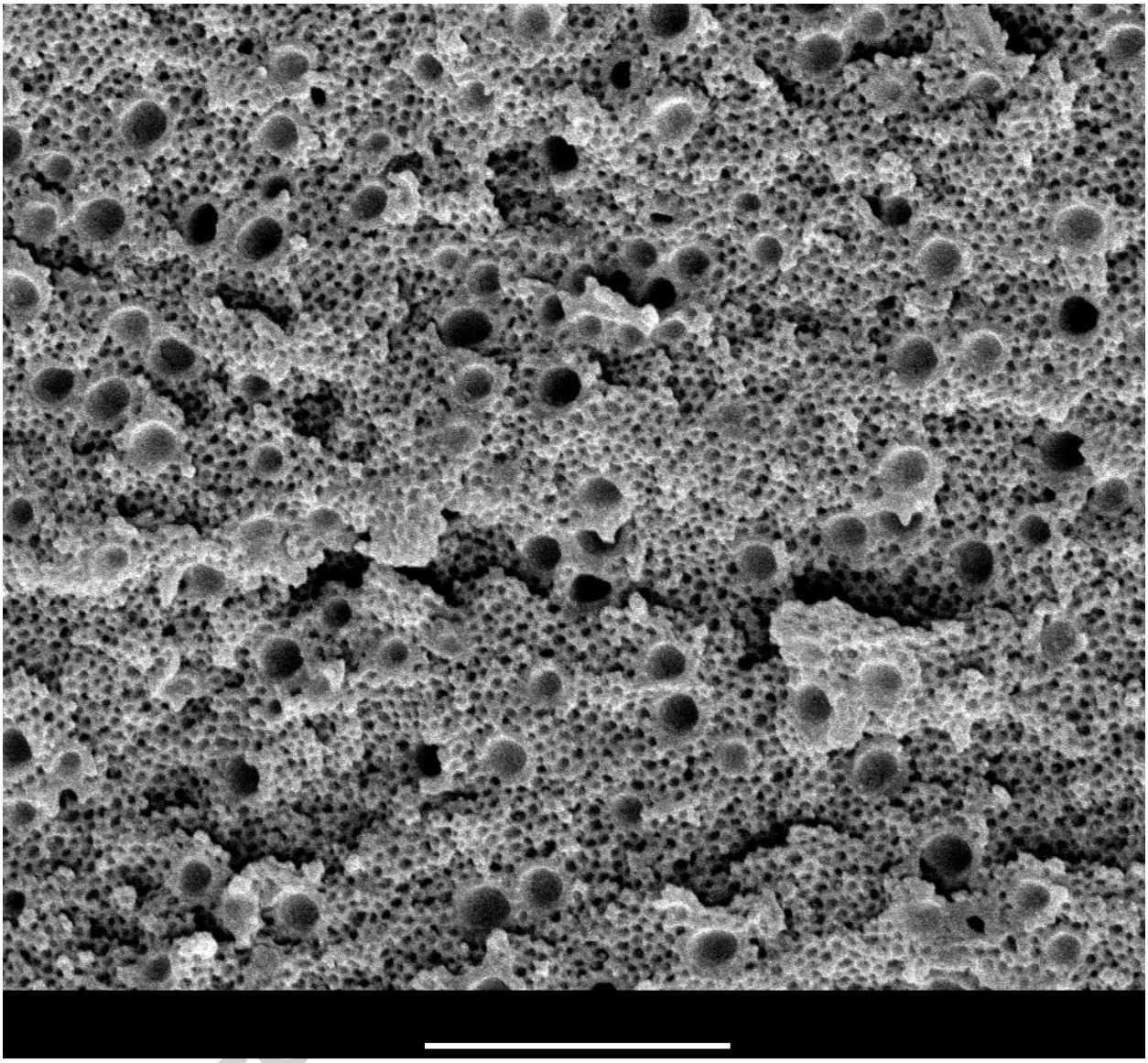

(a) 0.05 mm BGT

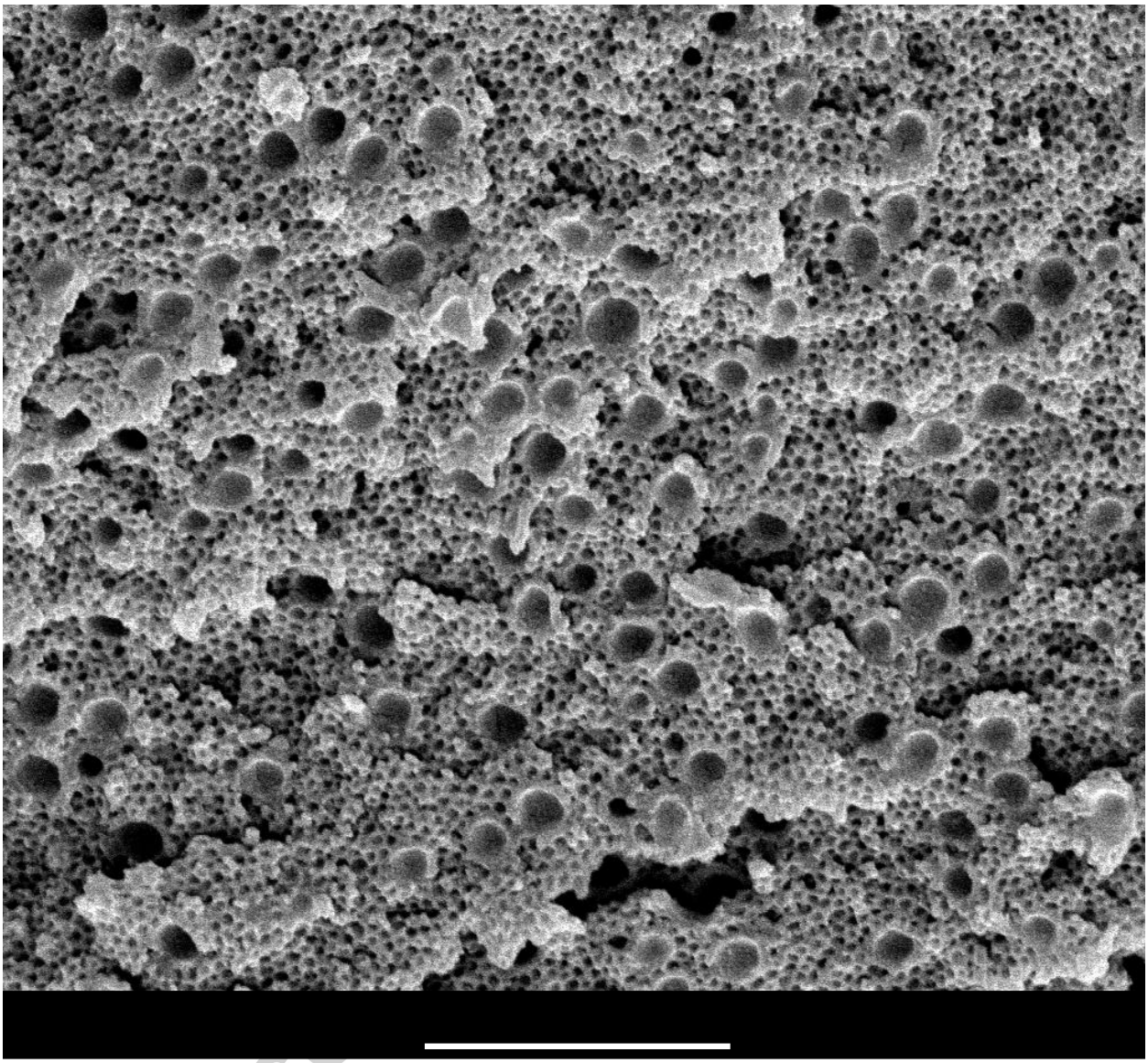

(b) 1.6 mm BGT

Figure 8: Typical SEM images of the fracture surfaces.

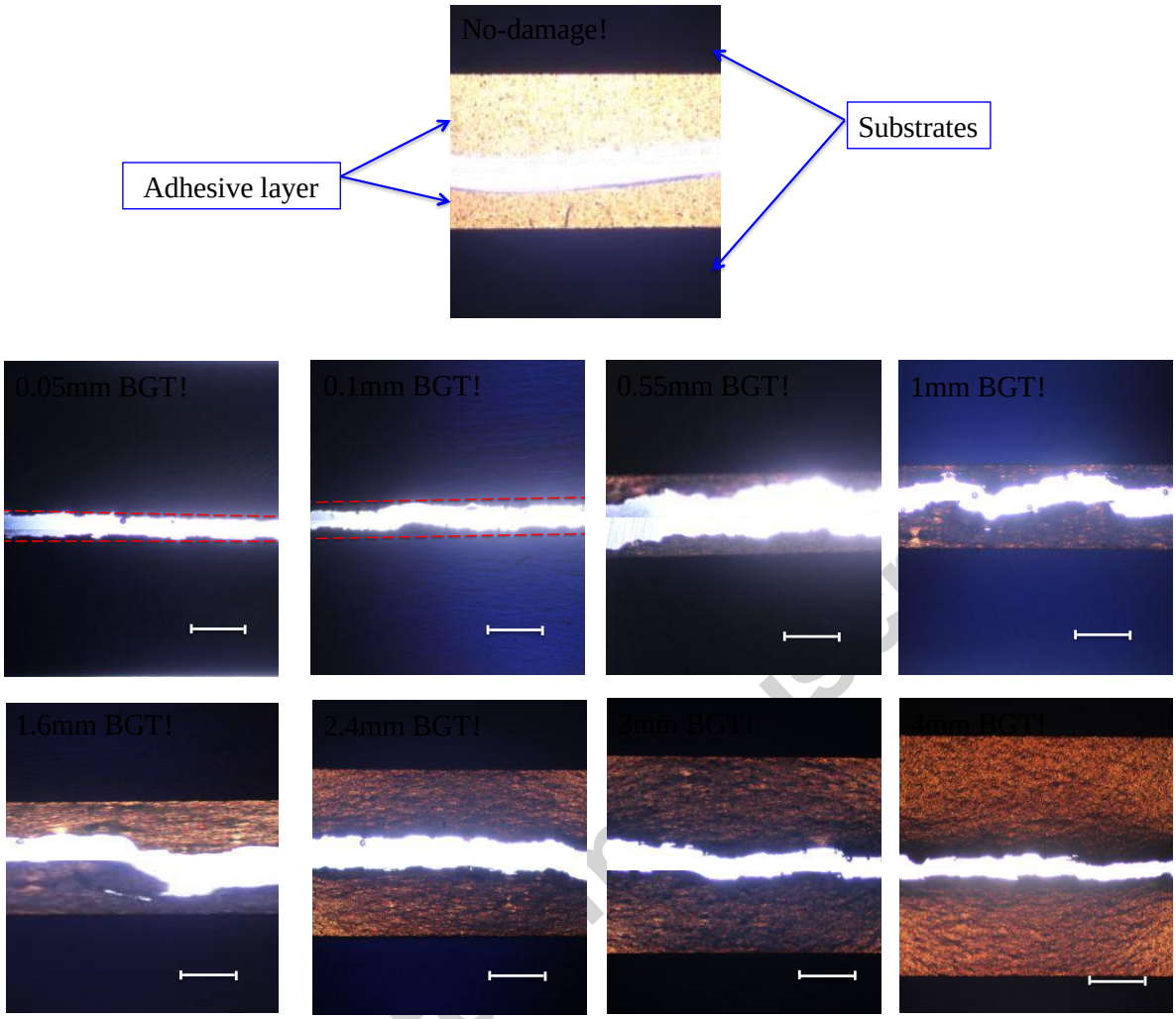

Figure 9: TOM images of the samples taken from Position-a. The top image is for a sample without any damage in the adhesive layer which is taken from the PTFE insert region. The red dashed lines in the images for BGT 0.05 mm and 0.1 mm show the boundary between the substrates and the adhesive layer.

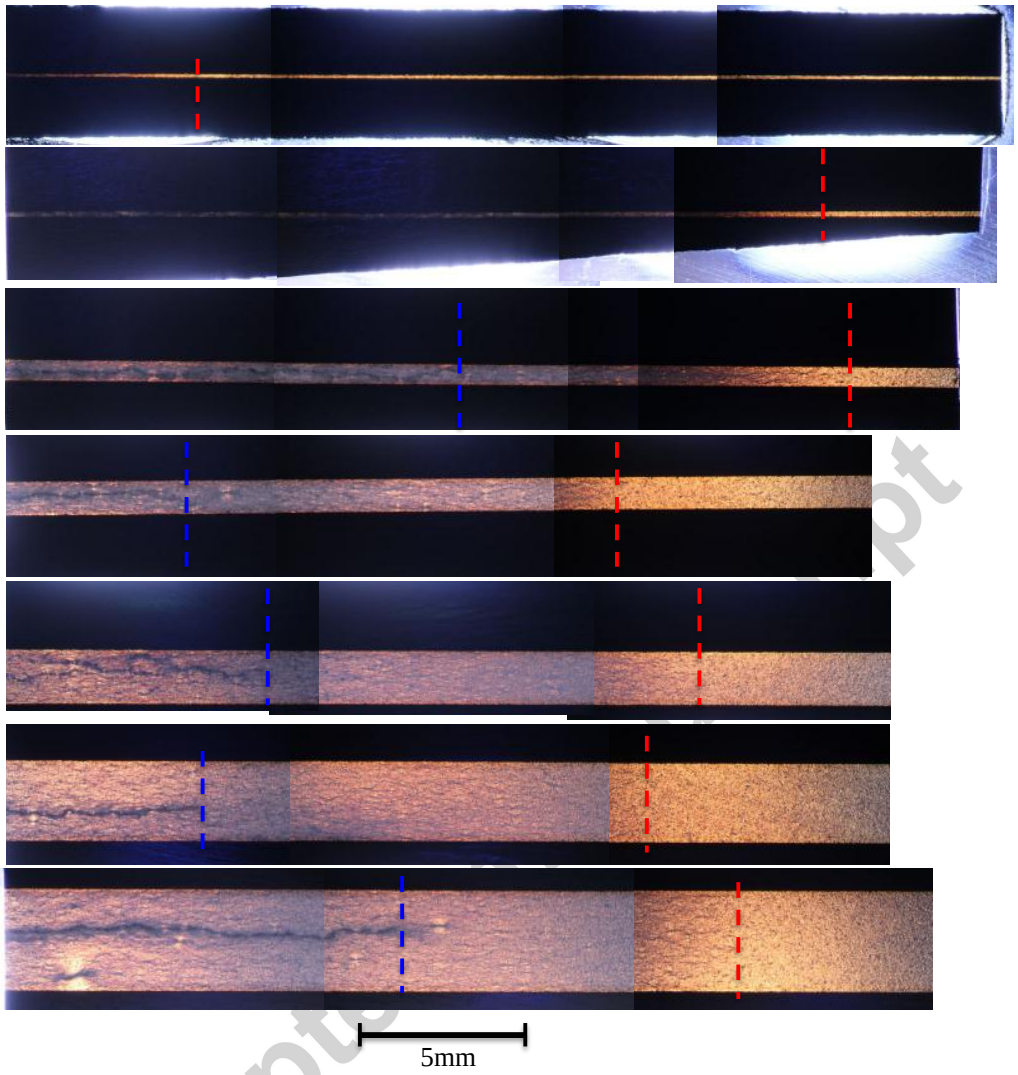

Figure 10: TOM images of the samples taken from Position-b under bright field. Crack growth direction is from left to right. The red dashed lines indicate the front of the PDZ and the blue dash lines indicate the crack tip.

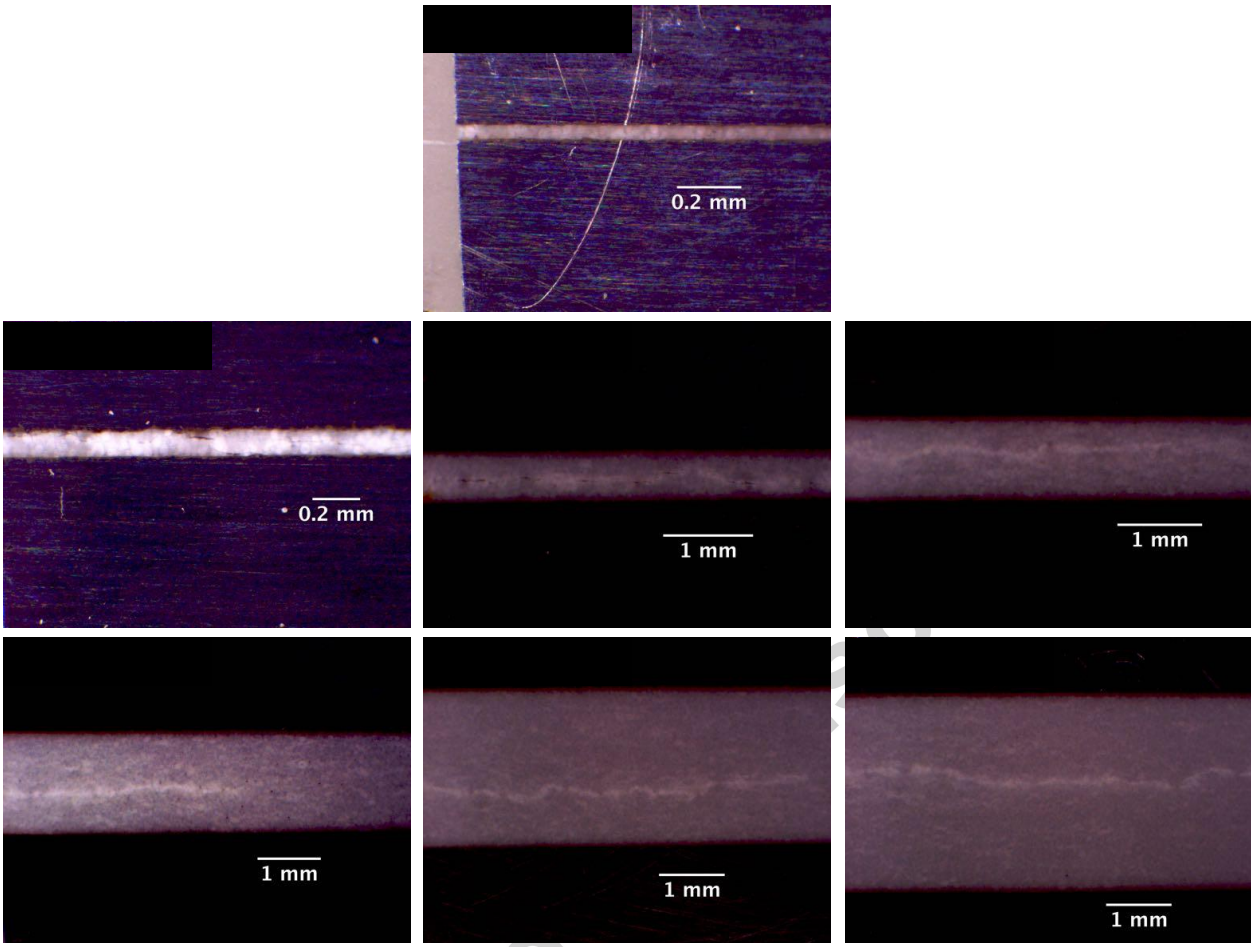

Figure 11: ROM images of the samples taken from Position-b in the TDCB specimens.

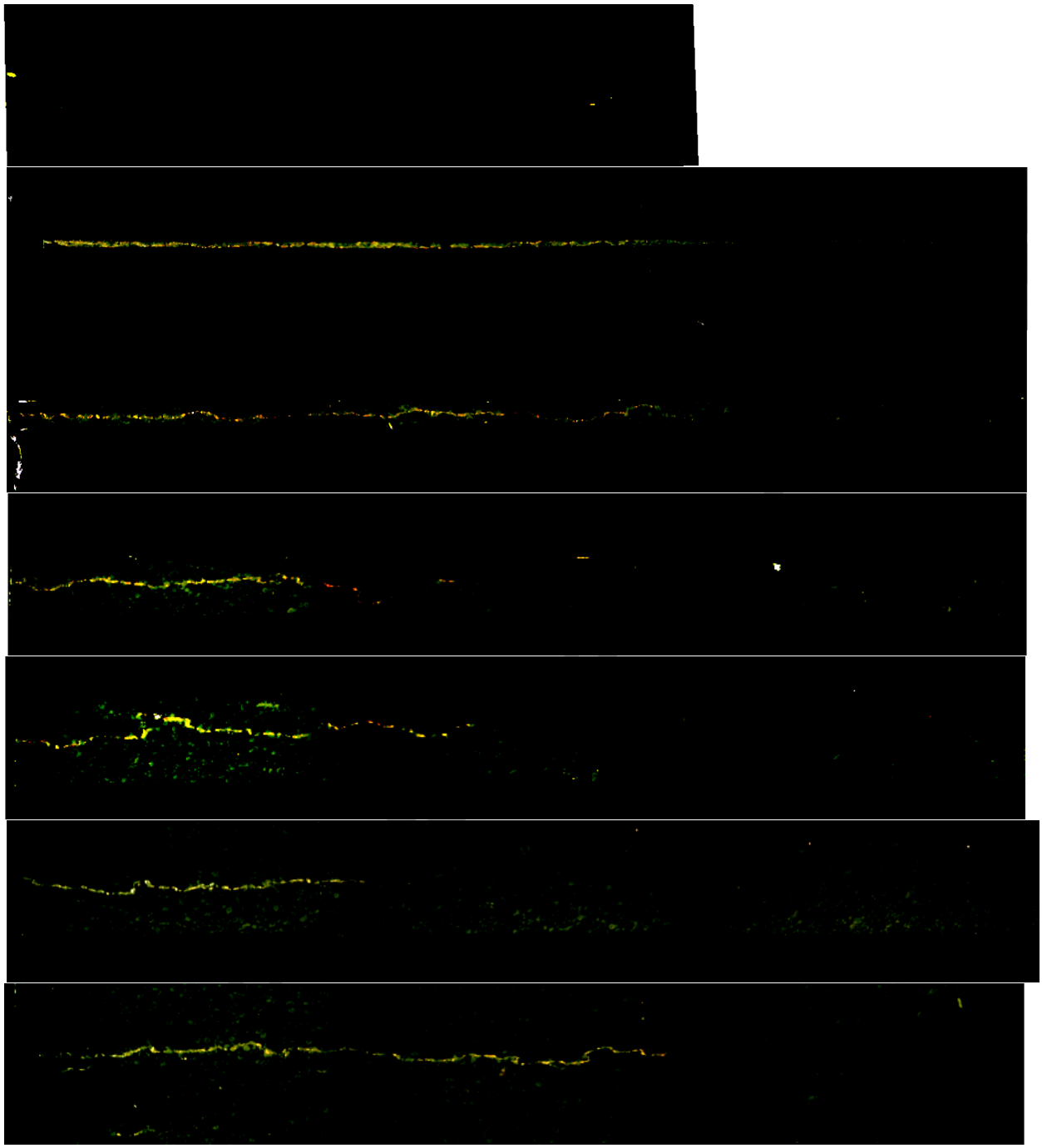

Figure 12: TOM images of the samples taken from Position-b under cross polarised light.

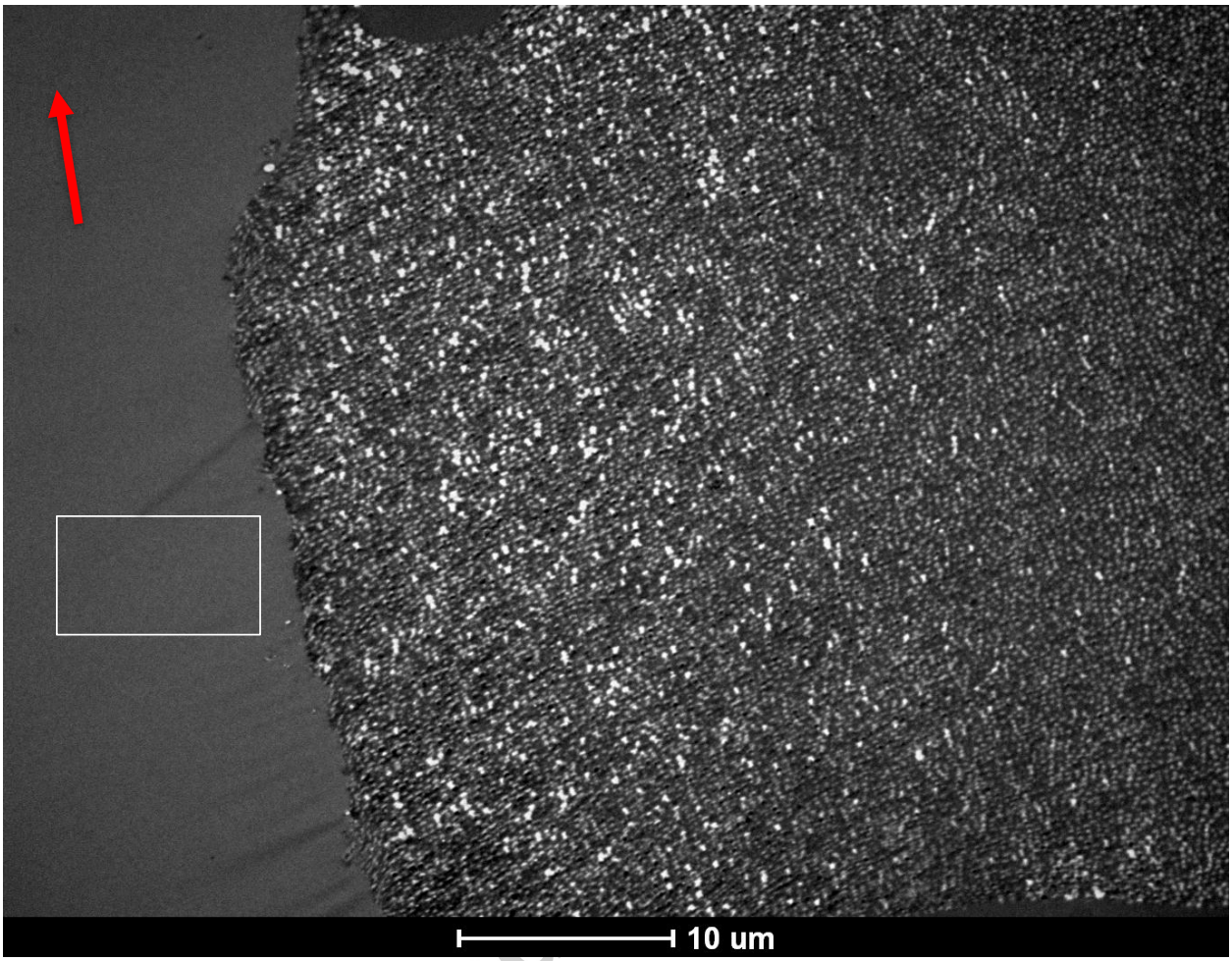

(a) 1 mm BGT

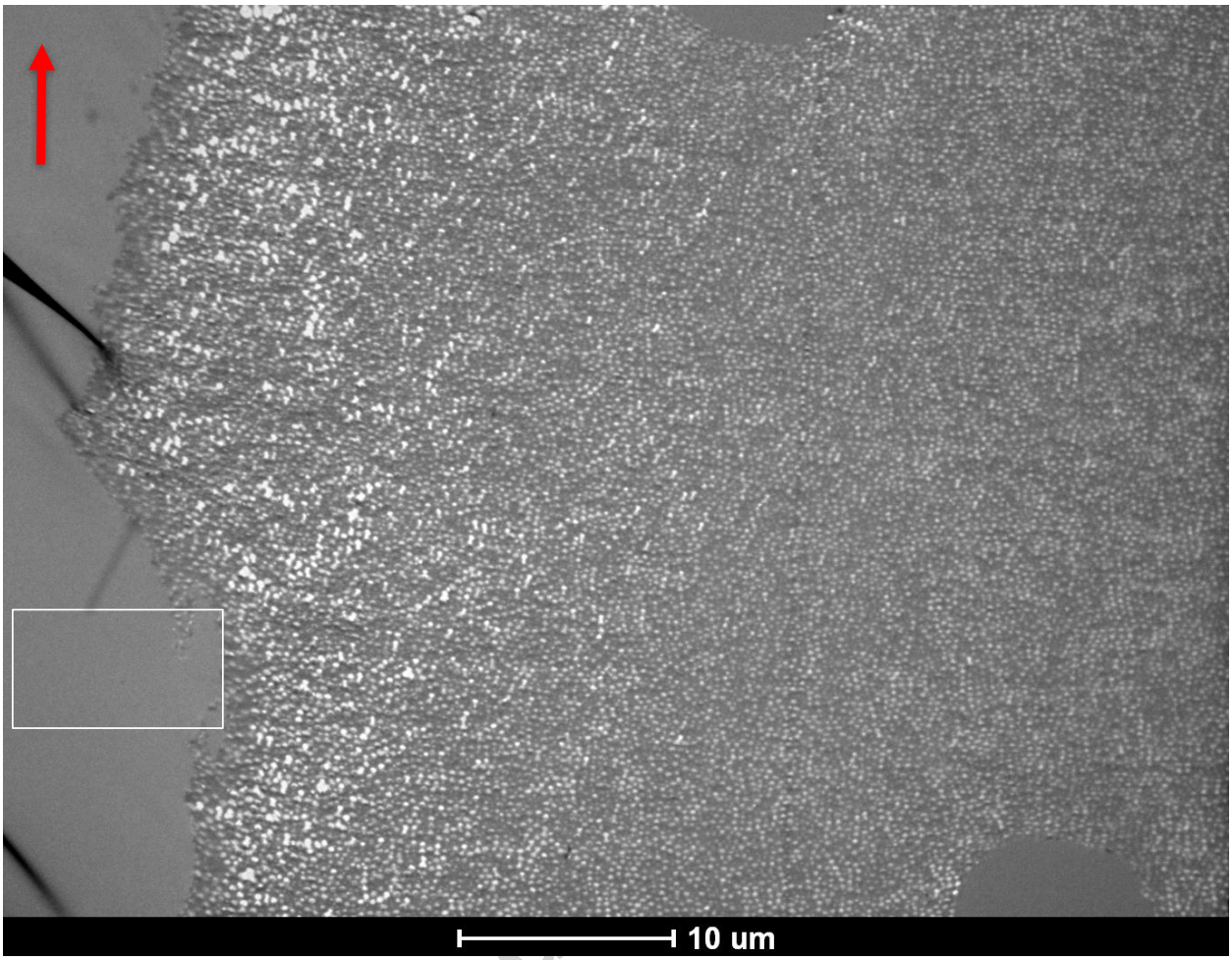

(b) 1.6 mm BGT

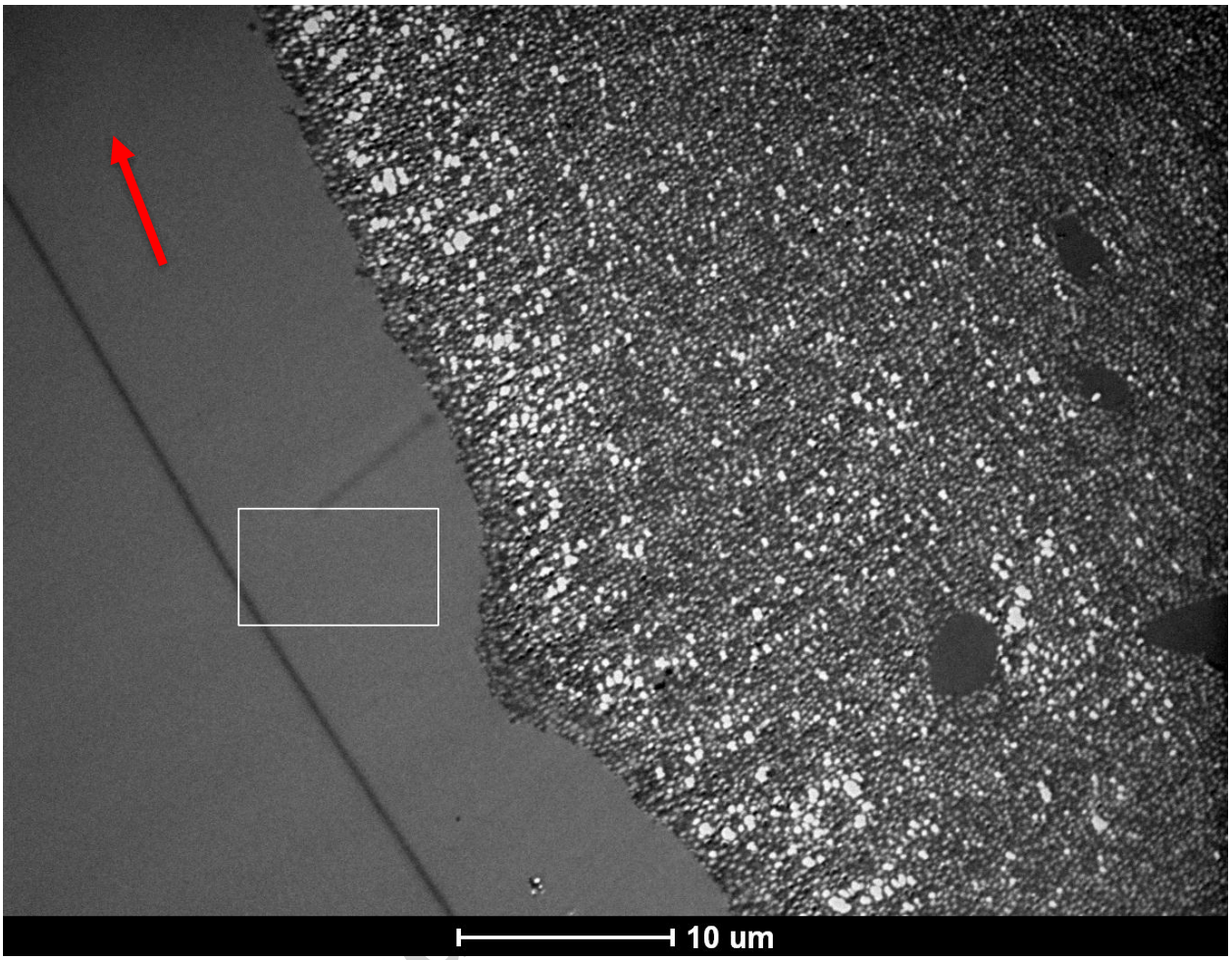

(c) 2.4 mm BGT

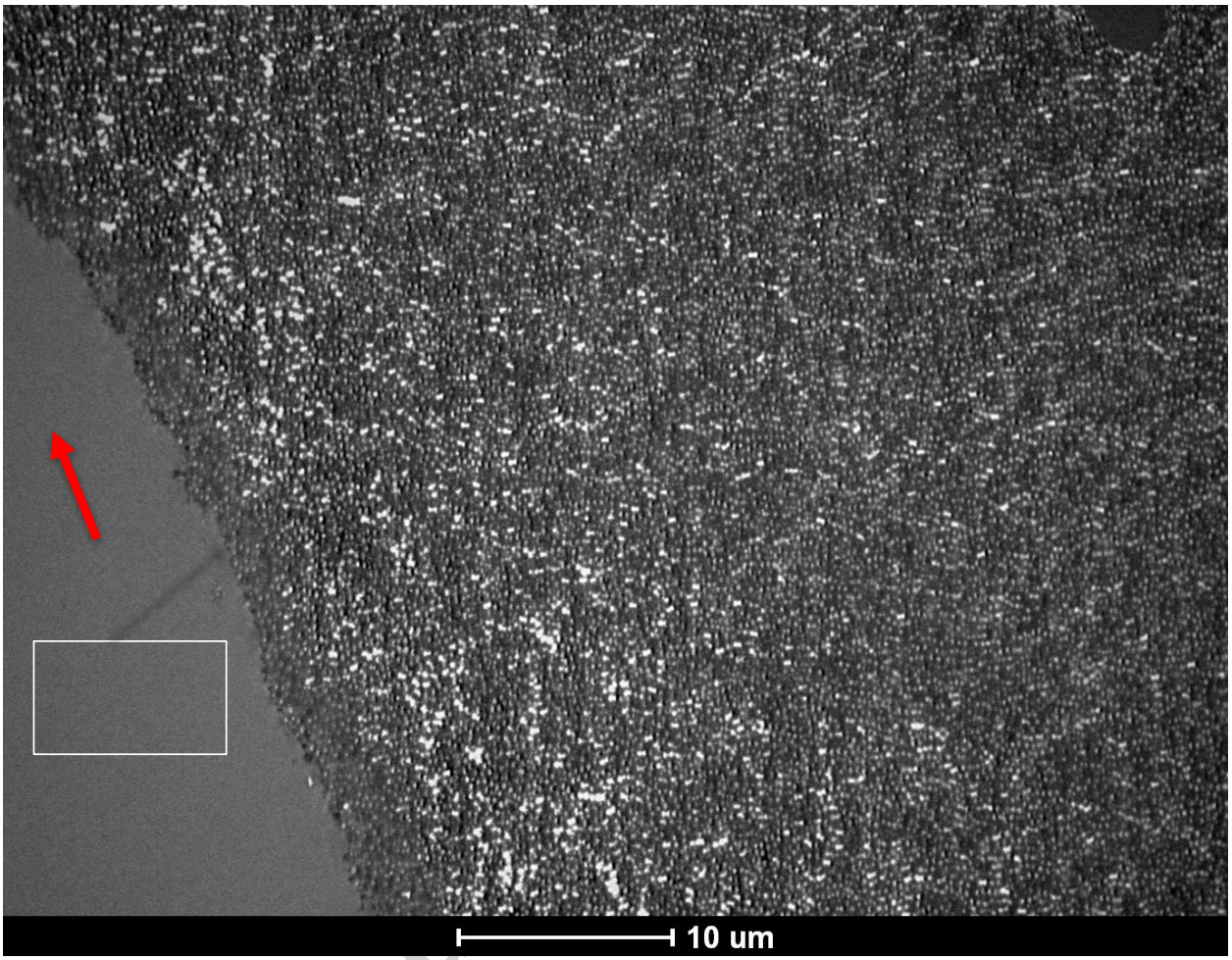

(d) 3 mm BGT

Figure 13: Typical TEM images of the fracture subsurface of the TDCB specimens. The red arrow indicates the microtoming direction.

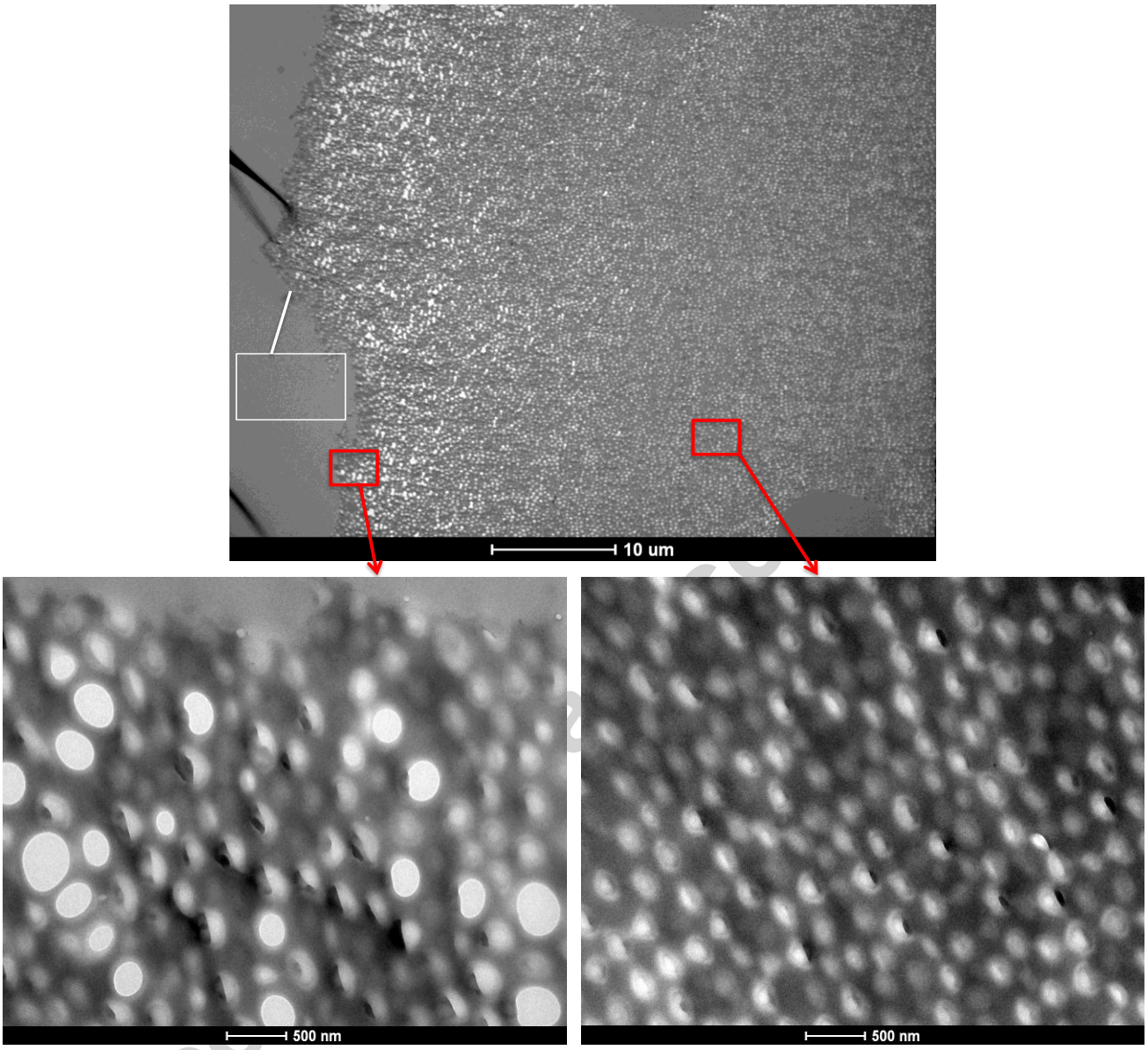

Figure 14: High magnification TEM images for a typical 1.6 mm BGT specimen.

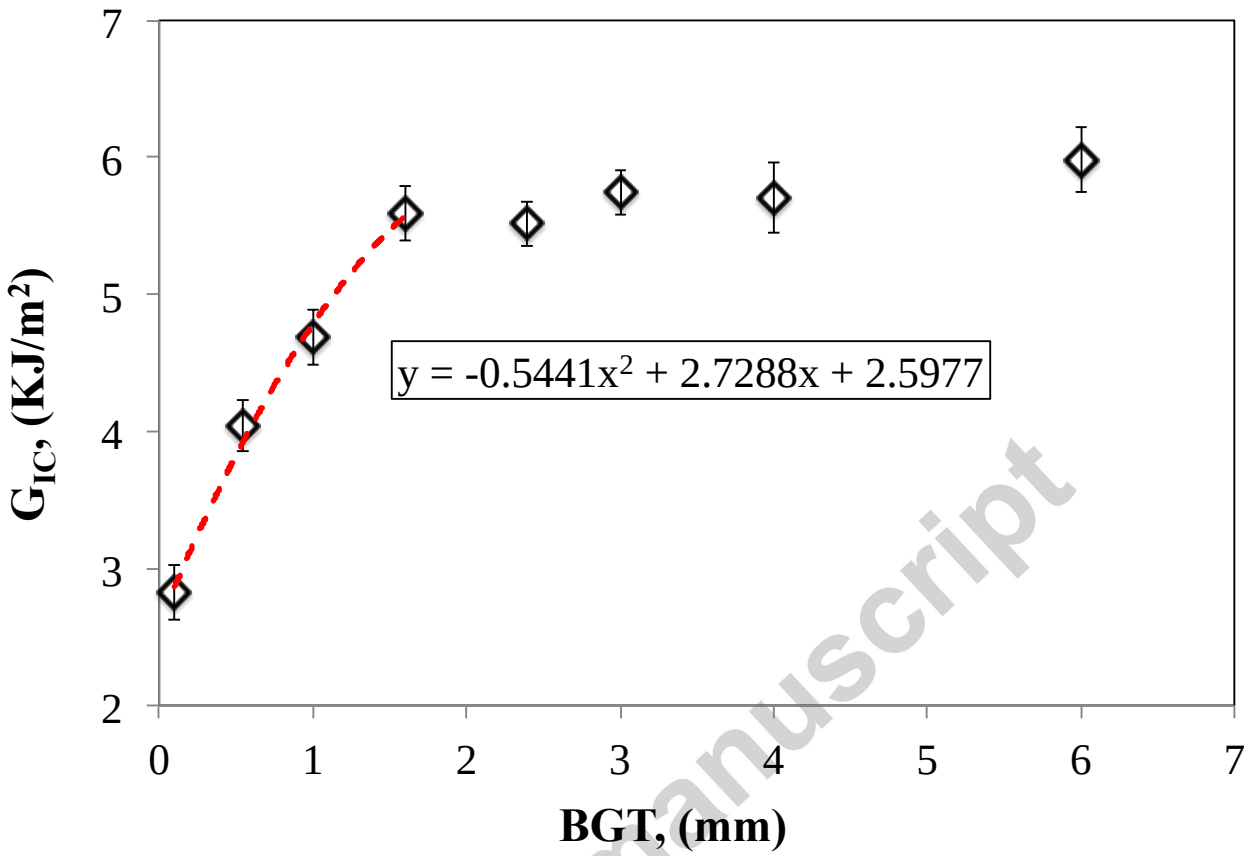

Figure 15: Polynomial fit of the G_{IC} versus BGT curve.

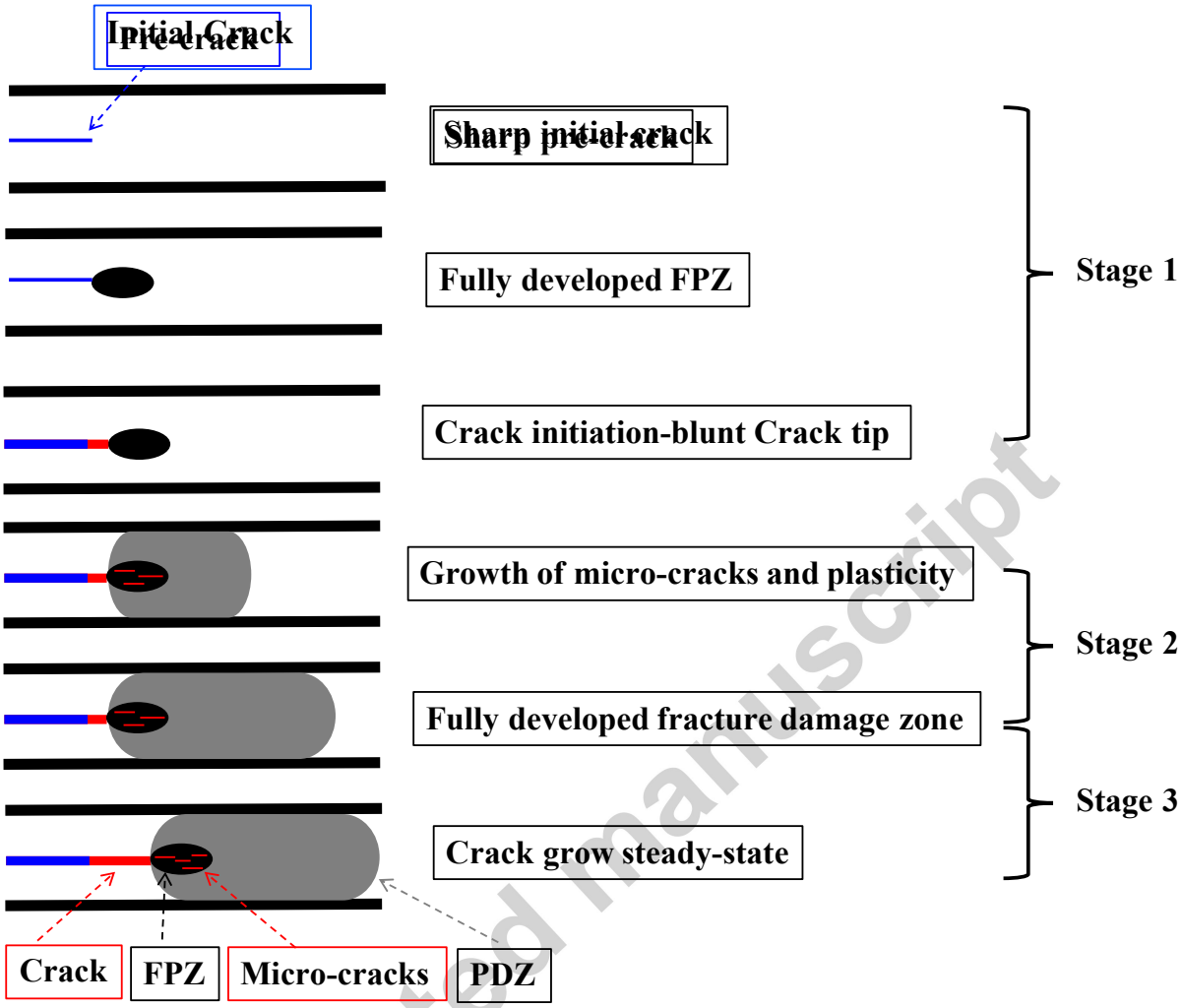

Figure 16: Fracture process evolution of the TDCB joints.